White Rose Research Online

eprints@whiterose.ac.uk
https://eprints.whiterose.ac.uk
Universities of Leeds, Sheffield and York

Deposited via The University of Leeds.

White Rose Research Online URL for this paper:
https://eprints.whiterose.ac.uk/id/eprint/236897/

Version: Published Version

Article:
Hajaliakbari, N., Head, D. and Harlen, O.G. (2026) Hydrodynamic interactions between pairs of sedimenting semi-flexible Brownian fibers. Physics of Fluids, 38. 013346. ISSN: 1070-6631

https://doi.org/10.1063/5.0301507

Reuse
This article is distributed under the terms of the Creative Commons Attribution (CC BY) licence. This licence allows you to distribute, remix, tweak, and build upon the work, even commercially, as long as you credit the authors for the original work. More information and the full terms of the licence here: https://creativecommons.org/licenses/

Takedown
If you consider content in White Rose Research Online to be in breach of UK law, please notify us by emailing eprints@whiterose.ac.uk including the URL of the record and the reason for the withdrawal request.

UNIVERSITY OF LEEDS
University of Sheffield
UNIVERSITY of York

Physics of Fluids

RESEARCH ARTICLE | JANUARY 22 2026

Hydrodynamic interactions between pairs of sedimenting semi-flexible Brownian fibers

Nasrollah Hajaliakbari ; David Head ; Oliver G Harlen

Check for updates

Physics of Fluids 38, 013346 (2026)
https://doi.org/10.1063/5.0301507

View Online Export Citation

Articles You May Be Interested In

A simulation platform for slender, semiflexible, and inextensible fibers with Brownian hydrodynamics and steric repulsion

Physics of Fluids (December 2024)

Large scale Brownian dynamics of confined suspensions of rigid particles

J. Chem. Phys. (December 2017)

Efficient Brownian Dynamics of rigid colloids in linear flow fields based on the grand mobility matrix

J. Chem. Phys. (May 2018)

27 January 2026 16:49:31

AIP Advances
Why Publish With Us?
21DAYS average time to 1st decision
OVER 4 MILLION views in the last year
INCLUSIVE scope
Learn More
AIP Publishing

AIP Publishing

Physics of Fluids ARTICLE pubs.aip.org/aip/pof

Hydrodynamic interactions between pairs of sedimenting semi-flexible Brownian fibers

Cite as: Phys. Fluids **38**, 013346 (2026); doi: 10.1063/5.0301507
Submitted: 9 September 2025 · Accepted: 16 December 2025 ·
Published Online: 22 January 2026

View Online Export Citation CrossMark

Nasrollah Hajaliakbari,[1,a] David Head,[1,b] and Oliver G Harlen[2,c]

AFFILIATIONS

[1]School of Computer Science, Faculty of Engineering and Physical Science, University of Leeds, Leeds, United Kingdom
[2]School of Mathematics, Faculty of Engineering and Physical Science, University of Leeds, Leeds, United Kingdom

[a)]Electronic mail: scnhv@leeds.ac.uk
[b)]Author to whom correspondence should be addressed: d.head@leeds.ac.uk
[c)]Electronic mail: o.g.harlen@leeds.ac.uk

ABSTRACT

The sedimentation of semiflexible fibers is a central process in the production of a range of important materials such as paper and fiber-reinforced composites. Predicting the dynamics of such fibers when both Brownian motion and hydrodynamic interactions are relevant, which would be a powerful tool to support the design of these materials, is nonetheless numerically challenging. Here, we utilize a computational framework that incorporates fiber elasticity, thermal fluctuations, and hydrodynamic interactions represented as Rotne–Prager–Yamakawa kernels and perform a parametric study of the simplest system in which hydrodynamic interactions are relevant, that is, pairs of fibers starting from one of two initial configurations. We also provide analytical predictions for the initial velocity and rotation of rigid fibers in the Oseen approximation. We systematically studied the systems in which bending, thermal fluctuations, and hydrodynamic interactions are included for the sedimenting semi-flexible fibers. Our goal was to determine when one of thermal fluctuations or hydrodynamics dominates over the other, or when both must be considered together, to inform the understanding and design of such systems. The short- and long-time dynamics of the fibers are thoroughly characterized, with good agreement with the analytical calculations for the initial behavior, and the observed trends are interpreted in terms of the underlying physical mechanisms. We finish with a discussion of the use of Rotne–Prager–Yamakawa kernels over alternative frameworks such as bead models and suggest potential directions for future work.

© 2026 Author(s). All article content, except where otherwise noted, is licensed under a Creative Commons Attribution (CC BY) license (https://creativecommons.org/licenses/by/4.0/). https://doi.org/10.1063/5.0301507

27 January 2026 16:49:31

I. INTRODUCTION

The sedimentation of fibers suspended in a viscous fluid is a key process in the production of materials such as paper and fiber-reinforced composites. Both the dispersion (mixing) and aggregation (flocculation) mechanisms of fibers during sedimentation can control the final grade of the finished product. These mechanisms have significant effects on a range of properties such as esthetics, brittleness, durability, strength, roughness, and uniformity.[1,2] Key material parameters for the fibers are their length, bending stiffness, aspect ratio, and any intrinsic curvature. For small fibers, it is also necessary to consider thermal fluctuations (Brownian motion), often quantified by the persistence length. Internal elastic forces are balanced by viscous friction with the fluid and the external field generated by gravity. In addition, to reliably predict the sedimentation of fiber assemblies, it is also essential to consider hydrodynamic interactions between fibers, as these can dominate the dynamics for nearby fibers. However, the combination of thermal fluctuations and hydrodynamic interactions is challenging to model for slender bodies such as fibers, making it difficult to provide a predictive capability for this important class of system.

The deformation of sedimenting fibers has been extensively investigated.[1,3–12] In 1996, Herzhaft *et al.*[6] performed experiments to evaluate the mean and variance of sedimentation velocity, plus the orientation distribution, for an aggregate of high-aspect-ratio fibers. They reported a steady-state condition for settling when the fibers were mostly aligned with the direction of gravity. A follow-on experimental study by the same group in 1999 attempted to identify the orientation distribution of settling non-Brownian, rigid fibers, in two regimes, dilute and semi-dilute.[7] It was found that as the concentration of fibers increased, more fibers tended to align with the direction of gravity. A challenge with the measurements was the tracking of fibers within the aggregate over long distances and times, as fibers could drift out of the

© Author(s) 2026

imaging plane due to fluctuations in the sedimentation velocity. Experimental studies also include that of Marchetti.,[9] who performed a detailed experimental study on the sedimentation of a flexible fiber for which the effects of Brownian motion could be neglected. It was shown that, depending on the ratio of the fiber stiffness to the strength of gravitational forces, a single sedimenting fiber adopts one of three steady state configuration regimes.[4] These regimes are "slightly-curved," "V," and "U" shapes, depending on the value of the dimensionless elasto-gravitational number (the ratio of elastic to gravitational forces), which was controlled in the experiments. In 2022, Cunha *et al.*[13] performed experiments in which Brownian motion also contributed to fiber deformation. It was found that Brownian effects measurably enhanced the deformation around the steady-state configuration compared to the equivalent non-Brownian fiber.

Parallel to these experimental investigations has been a growing body of research developing a range of analytical solutions and numerical tools to theoretically explore the sedimentation of flexible solids, including slender bodies, in a viscous fluid. In 1994, an analytical tool for the evaluation of the sedimentation regime with a degree of fiber deformation was proposed by Xu and Nadim. They predicted that, during sedimentation of a fiber within the viscous fluid, a torque would rotate the fiber toward a horizontal preferred state, perpendicular to the direction of settling.[3] Bead models have also been employed, in which the fiber is modeled as a string of beads rather than a continuous cylinder. The sedimentation of rigid, non-straight fibers comprised of three non-coplanar segments has been investigated by Tozzi *et al.*[11] and achieved partial agreement with experimental results, but was unable to accurately predict the drag force. A bead model was also employed by Cosentino Lagomarsino *et al.*[14] to observe differing sedimentation regimes, assuming a constant fiber length and ignoring thermal fluctuations. They showed that errors in predicting the bending amplitude (defined as the distance between the uppermost and the lowermost point of the filament along the direction of the applied force) were found to increase for high fiber aspect ratios (Fig. 1).

The gear model, a modified version of bead model, was suggested by Delmotte *et al.*[15] to include a series of touching beads, and to include non-local hydrodynamic interactions between beads using the fast multipole formulation of the Rotne–Prager–Yamakawa (RPY) tensor. It was found that the results deviated from an alternative numerical method (the joint model, for which the gap between two successive beads was higher than the gear model) at small values of the non-dimensional elasto-gravitational number. Slender body theory (SBT) is an alternative to bead modeling that incorporates hydrodynamic interactions as a distribution of singular forces along a continuous cylindrical object.[16] When applied to the sedimentation of fibers with both uniform and non-uniform cross sections, it predicts that the effects of initial configuration of a flexible filament are significant: fibers aligned with the direction of sedimentation are more susceptible to a buckling instability than those in a perpendicular alignment.[10] Recently, the sedimentation of an active poroelastic filament has been studied by a bead-spring model. It was found that this fiber can follow an out-of-plane zigzag pattern during the sedimentation.[17]

Hydrodynamic interactions between fibers have been modeled by both bead models and SBT. Llopis *et al.*[18] represented two fibers as bead chains with hydrodynamic interactions mediated by the Oseen tensor and evaluated short and long time sedimentation dynamics and fiber deformation for three classes of initial fiber geometry. Saggiorato *et al.*[19] used both continuum model and Oseen tensor to study the sedimentation of one, two, and three semiflexible non-Brownian filaments. The aspect ratio of fibers was not high. They found that individuals in a top-bottom pair (either co-planar or rotated) attract to each other due to the hydrodynamic interaction. Gustavsson and Tornberg[20] introduced a numerical tool to simulate non-Brownian rigid fibers, which was based on the non-local slender body approximation. Their results showed that the average velocity of multiple fibers was higher than an individual fiber and that the mean sedimentation dynamics of fiber clusters was very sensitive to randomness in the initial configuration. Nazockdast *et al.*[21] combined Stokeslets and rotlets in a model that did not incorporate Brownian motion and applied it to a toroidal arrangement of fibers, demonstrating the eventual loss of stability and formation of smaller tori. The Euler–Bernoulli beam theory was employed to solve the solid model. The deformation and breakup of a cloud of rigid fibers were investigated both experimentally and numerically by Park *et al.*[22] They used two different approximations for the far-field hydrodynamics, the so-called "fiblet," based upon point–particle interactions, and a more rigorous calculation based on SBT. The results were compared to the experimental data. The authors found that due to particle anisotropy, the breakup in the cloud of the rigid fibers is accelerated relative to the cloud of spherical particles.

Sedimenting rings have also been simulated within the Rotne–Prager–Yamakawa approximation,[23] demonstrating various modes of sedimentation depending on the initial configuration and the ring flexibility. The results obtained from experiments supported by a numerical tool have demonstrated that, during the sedimentation, knotted loops can attain a flat, wide, and thin toroidal form, with a number of intertwined loops oriented perpendicularly to gravity.[24] For such a structure, the individual loops periodically swirl around each other, while a much slower rotation of the entire system around the vertical symmetry axis was observed. Bukowicki and Ekiel-Jezewska[25] studied the sedimentation of a pair of both rigid and flexible non-Brownian fibers with both initial alignment of symmetric and non-symmetric with respect to a vertical plane, by the use of the Rotne–Prager–Yamakawa (RPY) approximation. They found that rigid rods exhibit

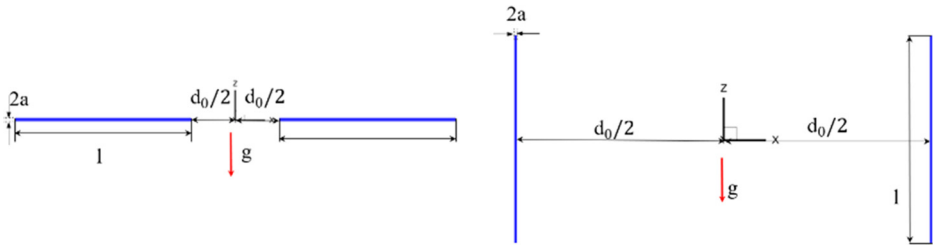

FIG. 1. A representation of geometric parameters for initially collinear (left image) and side-by-side (right image) configurations of two pairs of flexible fibers. The direction of gravity is also shown.

27 January 2026 16:49:31

© Author(s) 2026

symmetric periodic orbits as they are sedimenting, while for flexible pairs, it depends on the initial alignment. They only reported the changes in the alignments of fibers, but not the distance between fibers in a pair. Mostly, it was found that the flexible fibers tend to converge toward horizontal and parallel orientation, as previously reported in Ref. 19. Very recently, Maxian and Donev considered the hydrodynamic interactions for a pair and a cluster of Brownian fibers with the use of RPY kernels.[26] It was shown that the fibers approach each other when the hydrodynamic interactions are strong enough compared to the Brownian motion. However, they only considered one set of parameters and initial configuration and did not report sedimentation velocity and fiber orientation.

To the best of our knowledge, there has been no parametric study of the hydrodynamic interactions between semiflexible fibers that undergo thermal fluctuations. The purpose of this paper is to employ the RPY framework of Maxian and Donev[26] to evaluate the short- and long-time dynamics of a sedimenting pair of semiflexible fibers, varying parameters such as fiber stiffness, the strength of thermal fluctuations, and the initial geometry of the fibers. This paper is organized as follows. In Sec. II, the problem is defined and key dimensionless parameters given. In Sec. III, the simulation methodology is described and the details of a continuum rigid rod calculation are given that is used to benchmark our results. In Sec. IV, we present our results, considering first the dynamical regime (thermal vs hydrodynamic dominated), then the short-time dynamics, and finally the long-time dynamics, as key independent parameters are systematically varied. We finish in Sec. V with a summary and discussion of our findings.

II. PROBLEM DESCRIPTION

In this paper, the sedimentation of two pairs of identical cylindrical fibers of length l, radius a, and bending stiffness k through a fluid of viscosity μ are considered, with the difference in density between the fibers and the fluid equal to $\Delta\rho$. The persistence length l_p is defined as

$$l_p = \frac{k}{k_B T},$$

with k_B the Boltzmann's constant and T the absolute temperature.

The dynamics of this problem can be described by three non-dimensional numbers describing the relative importance of gravity, fiber elasticity, and thermal fluctuations. These are the elasto-gravitational number (B^*), the dimensionless bending stiffness (κ), and the gravitational Peclet number (Pe_g), defined by

$$B^* = \frac{\Delta\rho g l^3}{k}, \tag{1}$$

$$\kappa = \frac{l_p}{l} = \frac{k}{k_B T l}, \tag{2}$$

$$Pe_g = \frac{2\pi a^3 \Delta\rho g l}{3 k_B T}, \tag{3}$$

where g is the gravitational constant. Note only two of these are independent; the choice of which to present will depend on context. In addition, two geometric ratios are also used, the ratio of the initial distance between fibers (see below) to their length (D^*) and the fiber aspect ratio ϵ, plus a non-dimensional time ($\bar{t}$), defined as

$$D^* = \frac{d_0}{l}, \tag{4}$$

$$\epsilon = \frac{a}{l}, \tag{5}$$

$$\bar{t} = \frac{t\Delta\rho g}{\mu l}. \tag{6}$$

Two different initial configurations are considered: one in which the fibers are aligned in a collinear horizontal configuration (here and below, "horizontal" means perpendicular to the direction of gravity), and a second side-by-side configuration where the fibers are separated horizontally but orientated vertically. A schematic description of these configurations is shown in Fig. 1.

III. METHODOLOGY

The dynamics of this system will primarily be studied numerically using the simulation tool developed by Maxian *et al.*[27,28] This code uses Rotne–Prager–Yamakawa (RPY) kernels to approximate the hydrodynamic interactions between fibers. A key advantage of this is that the resulting hydrodynamic mobility matrix is symmetric positive definite (SPD), a property required for the inclusion of Brownian motion.

To provide further insight, we also consider a simplified analytical model based on the Oseen approximation to determine the hydrodynamic interactions between the fibers in the initial phase of sedimentation.

A. Numerical method (Rotne–Prager–Yamakawa kernels)

The simulation code developed by Maxian *et al.*,[27,29] models the motion of semi-flexible fibers suspended in a viscous fluid by solving the Stokes' equations between a set of inextensible fibers subject to local force densities due to gravity and elasticity and the constraint that the fibers are inextensible. A full description of the methodology is provided by Maxian *et al.*[27–29]

1. Kinematic description of fiber motion

The centerline of each fiber is described mathematically by a continuous function, $\mathbb{X}(s,t)$, with s the distance along the contour, $0 \le s \le l$. This can be obtained by integrating along the tangent vector $\mathbb{T}(s) = \frac{\partial}{\partial s}\mathbb{X}$ from the position of fiber midpoint $\boldsymbol{X}_{MP}$ (the discretized distribution of $\mathbb{X}$, evaluated at the midpoint MP, $s = l/2$), that is,

$$\mathbb{X}(s,t) = \boldsymbol{X}_{MP}(t) + \int_{\frac{l}{2}}^{s} \mathbb{T}(s',t)ds'. \tag{7}$$

In the simulation, the fiber profile is approximated by a type 2 Chebyshev polynomial that interpolates through m_x distinct points connected by m tangent vectors interpolated by a type 1 Chebyshev polynomial ($m_x = m + 1$). This discretized representation is referred to as the set of points $\boldsymbol{X}$, related to the midpoint and the tangent vectors $\boldsymbol{\tau}$ by the invertible matrix $\boldsymbol{\chi}$,

$$\boldsymbol{X} = \boldsymbol{\chi}\begin{pmatrix} \boldsymbol{\tau} \\ \boldsymbol{X}_{MP} \end{pmatrix}. \tag{8}$$

27 January 2026 16:49:31

© Author(s) 2026

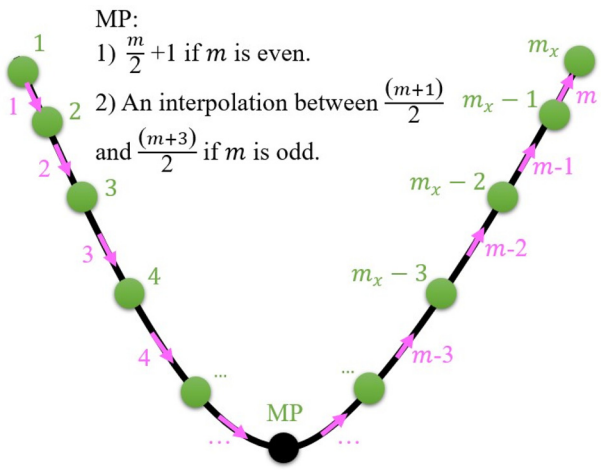

FIG. 2. The configuration of a discretized fiber described by Chebyshev points $\boldsymbol{X}$ (green and black solid circles) and tangent vectors $\boldsymbol{\tau}$ (magenta arrows). The solid black line represents the continuous profile of the fiber, $\mathbb{X}$ (Chebyshev interpolant).

These points and the fiber profile are illustrated in Fig. 2. Note that the points are not uniformly distributed along the fiber. The operator $\boldsymbol{\chi}$ is used to map between tangent vectors and positions, defined as

$$\boldsymbol{X} = \begin{pmatrix} \boldsymbol{D}^{\dagger}_{m+1}\boldsymbol{E}_{m\to m+1} & \boldsymbol{B} \end{pmatrix} \begin{pmatrix} \boldsymbol{\tau} \\ \boldsymbol{X}_{MP} \end{pmatrix} := \boldsymbol{\chi}\bar{\boldsymbol{\tau}}. \tag{9}$$

The first parenthesis acts as an operator. The second parenthesis is the operand, which includes the tangent vectors plus the midpoint. The matrix $\boldsymbol{B}$ in the first parenthesis is defined such that $\boldsymbol{X}_{MP}$ is the middle point (midpoint) of $\boldsymbol{X}$ on m_x Chebyshev grid number. The superscript † shows the pseudo-inverse of the differentiation matrix $\boldsymbol{D}$. The subscript of $\boldsymbol{D}$ shows that this operation must be done on the grid of size $m+1$, that is, m_x (shown in Fig. 1). The extension matrix $\boldsymbol{E}$ takes the tangent vectors from a grid of size m into one of size m_x. The inverse of operator $\boldsymbol{\chi}$ differentiates $\boldsymbol{X}$ on the grid size m_x and then downsamples to the grid size of m via the matrix $\boldsymbol{E}_{m+1\to m}$.

By differentiating Eq. (7), we obtain an equation of motion for the positions of each fiber relative to the midpoint velocity $\boldsymbol{U}_{MP}$,

$$\partial_t \boldsymbol{X}(s,t) = \boldsymbol{U}_{MP}(t) + \int_{\frac{L}{2}}^{s} \partial_t \boldsymbol{\tau}(s',t)ds'. \tag{10}$$

Since the fiber is constrained to be inextensible, the rate of change of the tangent vectors must be in the form of a rotation

$$\partial_t \boldsymbol{\tau} = \boldsymbol{\Omega} \times \boldsymbol{\tau} = -\mathbf{C}\boldsymbol{\Omega}, \tag{11}$$

where $\mathbf{C}$ is a matrix corresponding to this set of rotations. Hence, the change in the position of the points $\boldsymbol{X}$ is described by a linear kinematic discrete operator $\boldsymbol{K}$, which operates on the set of local tangent rotations $\boldsymbol{\Omega}$, and fiber midpoint velocity $\boldsymbol{U}_{MP}$, which we collectively write as $\boldsymbol{\alpha} = (\boldsymbol{\Omega}, \boldsymbol{U}_{MP})$,

$$\partial_t \boldsymbol{X}(s) := \boldsymbol{K}\boldsymbol{\alpha} = \boldsymbol{\chi}\begin{pmatrix} -\boldsymbol{C} & 0 \\ 0 & \boldsymbol{I} \end{pmatrix}\begin{pmatrix} \boldsymbol{\Omega} \\ \boldsymbol{U}_{MP} \end{pmatrix}. \tag{12}$$

In Eq. (12), we define a pseudo-inverse of $\boldsymbol{K}$ as

$$\boldsymbol{K}^{-1} = \begin{pmatrix} -\boldsymbol{C} & 0 \\ 0 & \boldsymbol{I} \end{pmatrix}\boldsymbol{\chi}^{-1} = \bar{\boldsymbol{C}}^{T}\boldsymbol{\chi}^{-1}. \tag{13}$$

Note the $\boldsymbol{K}^{-1}$ is not the true inverse of $\boldsymbol{K}$ but can be written as

$$\boldsymbol{K}^{-1}\boldsymbol{K} = \begin{pmatrix} -\boldsymbol{C}^2 & 0 \\ 0 & \boldsymbol{I} \end{pmatrix} \to \bar{\boldsymbol{C}}^{T}\boldsymbol{K}^{-1}\boldsymbol{K} = \bar{\boldsymbol{C}}. \tag{14}$$

The constraint of inextensibility is enforced by tensions $\boldsymbol{\lambda}$ along each fiber that prevent changes in the length of the tangent vectors. This is done by imposing that there is no energy dissipation resulting from these constraint force, i.e.,

$$\langle \boldsymbol{\lambda}, \partial_t \boldsymbol{X} \rangle = \langle \boldsymbol{\lambda}, \boldsymbol{K}\boldsymbol{\alpha} \rangle = \langle \boldsymbol{K}^{*}\boldsymbol{\lambda}, \boldsymbol{\alpha} \rangle = 0. \tag{15}$$

Here, $\boldsymbol{K}^{*}$ is the adjoint to the matrix $\boldsymbol{K}$, which for the discretized system is its transpose. The angled brackets $\langle \cdot, \cdot \rangle$ denote the standard inner product. This equation imposes the requirement that the internal forces ($\boldsymbol{\lambda}$) cannot add or deduct energy from the system.

2. Non-Brownian fiber formulations (deterministic formulation)

For clarity, the governing equations in the absence of Brownian motion, i.e., the deterministic formulation, are described first. The linearity of the Stokes equations means that the motion of the fibers is linearly related to the sum of force densities acting on them through the mobility operator $\mathbb{M}[\mathbb{X}]$ (which depends on the current configuration of the fibers),

$$\partial_t \mathbb{X}(s,t) = \mathbb{M}[\mathbb{X}]\mathbb{f}. \tag{16}$$

Here, $\mathbb{f}$ is made up of the sum of the gravitational, bending, and tension force densities. The bending force density is proportional to the fourth derivative of the continuous fiber profile with respect to arc length s, i.e., $\mathbb{f}^{k} = -k\partial_s^4 \mathbb{X}$, where k is the bending stiffness of the fiber. Together with the inextensibility condition, a saddle point system is formed that in the continuous case would be

$$\begin{pmatrix} -\mathbb{M}[\mathbb{X}] & \mathbb{K} \\ \mathbb{K}^{*} & 0 \end{pmatrix}\begin{pmatrix} \boldsymbol{\lambda} \\ \boldsymbol{\alpha} \end{pmatrix} = \begin{pmatrix} \mathbb{M}[\mathbb{X}]\left(\mathbb{f}^{k} + \mathbb{f}^{g}\right) \\ 0 \end{pmatrix}, \tag{17}$$

with $\mathbb{f}^{g}$ the gravitational force density. The equivalent discretized system is

$$\begin{pmatrix} -\widetilde{\boldsymbol{M}} & \boldsymbol{K} \\ \boldsymbol{K}^{T} & 0 \end{pmatrix}\begin{pmatrix} \boldsymbol{\lambda} \\ \boldsymbol{\alpha} \end{pmatrix} = \begin{pmatrix} \widetilde{\boldsymbol{M}}(-\boldsymbol{L}\boldsymbol{X} + \boldsymbol{F}^{g}) \\ 0 \end{pmatrix}, \tag{18}$$

where $\widetilde{\boldsymbol{M}}$ is the symmetric positive definite discrete mobility matrix and $\boldsymbol{L}$ is the matrix operator corresponding to the bending force, $\boldsymbol{F}^{k} = -\mathbf{L}\mathbf{X}$, in the discretized system.

We can now eliminate the constraints $\boldsymbol{\lambda}$ to leave the following equation for the deterministic dynamics of the system:

$$\partial_t \boldsymbol{X} = -\boldsymbol{N}(\boldsymbol{L}\boldsymbol{X} - \boldsymbol{F}^{g}), \tag{19}$$

$$\boldsymbol{N} = \boldsymbol{K}\left(\boldsymbol{K}^{T}\widetilde{\boldsymbol{M}}^{-1}\boldsymbol{K}\right)^{\dagger}\boldsymbol{K}^{T}. \tag{20}$$

Here, the matrix $\boldsymbol{N}$ is the mobility matrix projected onto the space of inextensible motions, and the superscripts $\boldsymbol{T}$ and † denote the transpose and adjoint operations, respectively.

27 January 2026 16:49:31

© Author(s) 2026

3. Brownian fiber formulations

Having determined the equation governing the deterministic dynamics, we can now form the corresponding Langevin equation. To satisfy the fluctuation–dissipation theorem, the covariance of the noise must be equal to $2k_BTN$, meaning that the coefficients must be proportional to some matrix $N^{\frac{1}{2}}$ satisfying

$$N^{\frac{1}{2}}(N^{\frac{1}{2}})^T = N. \tag{21}$$

It is worth noting that $N^{\frac{1}{2}}$ is not unique and only needs to satisfy the above relation. In addition, since the mobility N depends on the configuration of the fibers, the Ito form of the stochastic differential equations requires the inclusion of a drift term proportional to the divergence of N.[30] Thus, the Ito–Langevin equation is expressed in terms of X as[28,31]

$$\partial_t X = -NLX + NF^g + k_BT(\partial_X \cdot N) + \sqrt{2k_BT}N^{\frac{1}{2}}W(t), \tag{22}$$

where $W(t)$ is a vector of Gaussian white-noise processes (the formal derivatives of Brownian motion). Even in the presence of the drift term, the two-step integrator, which will be defined in Subsection III A 5, satisfies fluctuation–dissipation balance with respect to the constrained inextensible Gibbs–Boltzmann distribution.

4. Mobility matrix

The key computational challenge is to find an approximation for the mobility matrix M, which accounts for hydrodynamic interactions between fibers, that is, both sufficiently accurate and provides a computationally efficient means to calculate the terms in equation (18). Full details of the methodology used are given by Maxian and Donev.[26] For slender fibers, the fluid velocity of the fiber system can be formed by integrating over the singularity distribution along each fiber. In the high-aspect-ratio limit, the dominant contribution to the mobility comes from the self-term. In this approach, the fiber is modeled as an infinite series of regularized delta functions, referred to as blobs, and which are surface delta functions on spheres of radius $\hat{a}$ in the Rotne–Prager–Yamakawa (RPY) approximation. For the case in which these blobs are well separated ($R > 2\hat{a},$), the kernel is the sum of a Stokeslet and multipole doublet. However, when the blobs overlap ($R \leq 2\hat{a},$), the nonsingular kernel tends to the classical Stokes drag mobility $\frac{1}{6\pi\mu\hat{a}}$ as $x \to y$ in terms of the point y, where the force is spread by the regularized delta function, and x the point where the resulting fluid velocity field at another surface delta function is averaged.[26] The regularized Rotne–Prager–Yamakawa kernels for these nonlocal terms are given, in terms of the vector distance $R = R\hat{R}$ between Chebyshev points, by

$$M_{RPY}(x,y) = \frac{1}{8\pi\mu}\begin{cases} \left(\frac{I+\hat{R}\hat{R}}{R} + \frac{2\hat{a}^2}{3}\frac{I-3\hat{R}\hat{R}}{R^3}\right) & R > 2\hat{a}, \\ \left(\left(\frac{4}{3\hat{a}} - \frac{3R}{8\hat{a}^2}\right)I + \frac{R}{8\hat{a}^2}\hat{R}\hat{R}\right) & R \leq 2\hat{a}. \end{cases} \tag{23}$$

Here, $\hat{a} \approx 1.12\,a$ is the regularized radius and a is the radius of the fiber. By use of asymptotic analysis,[26,32] it can be shown that this choice of regularized radius gives the same mobility as slender body theory, but removes the singularity in the integrand found in slender body theory.

In Eq. (23), parameters $R = \| R \|$, $\hat{R} = R/\| R \|$, and $\hat{R}\hat{R}$, are distance vector length, normalized distance vector, and outer product of $\hat{R}$ with itself, respectively. An important property of the Rotne–Prager–Yamakawa (RPY) approximation is that the mobility matrix calculated by this approach is symmetric positive definite, which is required when the Brownian motion is considered so that the square root of mobility matrix can be formed. The integrals are evaluated by using an oversampled quadrature along with Chebyshev weights and 200 integration points along each fiber for all terms (except the self-term). For the self-term, the number of oversampled points can be reduced through the use of a special quadrature, while still preserving the accuracy of that integral.

However, the use of such a hybrid method results in a mobility matrix that is not guaranteed to be SPD, especially for large values of aspect ratio and number of Chebyshev points due to numerical errors. To address this, a reference oversampled mobility matrix is defined as

$$M = M_{ref} := \widetilde{W}^{-1} E_u^T W_u M_{RPY,u} W_u E_u \widetilde{W}^{-1}. \tag{24}$$

The subscript u indicates that this operation is performed on an upsampled grid with N_u points that is obtained by resampling the Chebyshev interpolant, and the matrix $\widetilde{W}$ is formed from the Chebyshev weights. To symmetrize the mobility matrix, the diagonal elements of reference mobility matrix are replaced by

$$M_{SQS} = \frac{1}{2}\left(M\widetilde{W}^{-1} + \widetilde{W}^{-1}M^T\right). \tag{25}$$

This allows us to define the non-local terms as

$$\widetilde{M} = M_{ref} - BDiag\{M_{ref}\} + BDiag\{M_{SQS}\}, \tag{26}$$

where $BDiag$ stands for the diagonal blocks (self-interaction terms) of the matrix $\widetilde{M}$. The details regarding the integration of mobility matrix for the evaluation of the velocity on each fiber can be found in Refs. 26 and 28.

5. Time integrator

The temporal discretization for solving the equations of Brownian fibers[28] uses a two-step integration scheme. For this methodology, it is necessary to compute the stochastic drift terms as they arise from the inextensibility constraints of the fibers, and therefore must be included to properly account for the dynamics.[28] First, an initial estimate of stochastic Brownian velocity is used to obtain a new configuration of the fibers at the midpoint of the time step. This updated configuration is then used to estimate the drift velocity and provide a more accurate estimate of the Brownian velocity, which is then used to solve the dynamic equations for the fiber configuration at the end of the time step. Further details of this scheme can be found in Sec. A.3 of the supplementary material.

B. Continuum model (analytical solutions)

As a consequence of the simplicity of the initial configuration, it is possible to provide analytical predictions for the initial velocity and rotation rates in the rigid-fiber limit within the Oseen approximation, neglecting thermal fluctuations.[18,33] Denoting the coordinates of points along the contours of fibers 1 and 2 by x^1 and x^2, respectively, the

27 January 2026 16:49:31

© Author(s) 2026

contribution to the fluid velocity at points along fiber 1, due to the presence of fibers 2, $\boldsymbol{u}^2(\boldsymbol{x}^1)$, etc., is given by

$$\boldsymbol{u}^2(\boldsymbol{x}^1) = \frac{1}{8\pi\mu}\int\left\{\frac{\boldsymbol{f}^2}{|\boldsymbol{x}^1-\boldsymbol{x}^2|}+\frac{([\boldsymbol{x}^1-\boldsymbol{x}^2]\cdot\boldsymbol{f}^2)(\boldsymbol{x}^1-\boldsymbol{x}^2)}{|\boldsymbol{x}^1-\boldsymbol{x}^2|^3}\right\}d\boldsymbol{x}^2, \quad (27)$$

where $\boldsymbol{f}^2$ is the force density acting at point $\boldsymbol{x}^2$ along the axis of fiber 2. Each initial configuration is now considered, in turn, with the superscripts 1 or 2 being dropped when the meaning is clear.

Here, it should be mentioned that the Oseen tensor only includes the first term of RPY when $R > 2\hat{a}$. The results will converge to each other when the fibers are far from each other, but, due to periodic boundary conditions used for RPY, this is not the case.

1. Horizontal (collinear) configuration

On the assumption that the fibers are of uniform thickness and density, in the initial configuration, the gravitational force per unit along the fiber will be uniform and given by $f = \frac{w}{l}$, where w is the buoyancy adjusted weight of the fiber and l the fiber length. The z-component of the velocity at each point of the left-hand fiber, due to the presence of the right-hand fiber is given after straightforward integration by

$$u_z(x, z=0) = \frac{f}{8\pi\mu}\log\left|\frac{d/2+l-x}{d/2-x}\right|, \quad (28)$$

where d is the separation distance between the fibers and log denotes the natural logarithm. The integrated z component of the whole fiber velocity with respect to x on the left-hand fiber is then

$$U_z = \frac{f}{8\pi\mu l}\left(d\log\left|\frac{(d+2l)d}{(l+d)^2}\right| + 2l\log\left|\frac{(2l+d)}{(l+d)}\right|\right). \quad (29)$$

Note this is just the velocity induced by hydrodynamic interactions with the other fiber; the net velocity will also include the sedimentation velocity of the fiber in isolation.

The net rotation rate ω of the left-hand side fiber can be similarly obtained by integration

$$\omega = \frac{12}{l^3}\int_{-\frac{l}{2}}^{\frac{l}{2}} q u_z(q) dq, \quad (30)$$

where $q = x - l/2$ is the distance to the center of the fiber and $u_z(q)$ the vertical velocity at that point as given by Eq. (20). This evaluates to

$$\omega = \frac{3f}{4\pi\mu l^3}\left[(l+d)(d)\log\frac{|d+l|}{|d|} + (l+d)(2l+d)\log\frac{|d+l|}{|d+2l|} + l^2\right]. \quad (31)$$

This rotation rate can be compared to the scale of rotation induced by thermal fluctuations, which derives from the rotational diffusivity D_r,[34]

$$D_r = \frac{3k_BT\log\left(\frac{l}{2a}\right)}{\mu\pi l^3}, \quad (32)$$

where k_B, T, and a are the Boltzmann constant, temperature, and radius of the fiber, respectively.

2. Vertical (side-by-side) configuration

Analogous to the previous geometry, the z-component of the velocity on each point of one fiber in the vertical fiber geometry due to the presence of the other is found to be

$$u_z(x=0,z) = \frac{f}{8\pi\mu}\left[2z\left(-\frac{1}{\sqrt{4d^2+(-2z+l)^2}}+\frac{1}{\sqrt{4d^2+(2z+l)^2}}\right) + l\left(\frac{1}{\sqrt{4d^2+(-2z+l)^2}}+\frac{1}{\sqrt{4d^2+(2z+l)^2}}\right)\right]. \quad (33)$$

The net z-component of the induced velocity on the whole fiber is obtained by the integration u_z of with respect to z, that is,

$$U_z(z) = \frac{f}{8\pi\mu l}\left(2\left(-d+\sqrt{d^2+l^2}\right)\right). \quad (34)$$

The x component of the induced velocity on the left-side fiber can be similarly found to be

$$u_x(z) = \frac{fd}{8\pi\mu}\left\{\frac{1}{\left[d^2+\left(z-\frac{l}{2}\right)^2\right]^{\frac{1}{2}}} - \frac{1}{\left[d^2+\left(z+\frac{l}{2}\right)^2\right]^{\frac{1}{2}}}\right\}. \quad (35)$$

Again, the rotation rate can be obtained by Eq. (30) with the modification that it now only depends on the x component of the velocity [defined as Eq. (35)], since that component is perpendicular to the fiber. As a result,

$$\omega = \frac{3fd}{2\pi\mu l^3}\left[2d - 2(d^2+l^2)^{\frac{1}{2}} + (l/2)\log\frac{\sqrt{d^2+l^2}+l}{\sqrt{d^2+l^2}-l}\right]. \quad (36)$$

IV. RESULTS

We now consider the interactions between two sedimenting fibers. In Stokes flow, an isolated straight rigid fiber at an inclined angle does not rotate, but sediments at an angle to the vertical. As a consequence, fibers inclined at different angles will move toward or apart from each other, even without thermal fluctuations or hydrodynamic interactions. Since our goal in this study is to highlight the competing roles of hydrodynamic interactions and Brownian motion, we deliberately chose initial geometries that were not inclined, i.e., were either horizontal or vertical, to eliminate this possibility from the early-time trajectories. Also, another reason that we selected these initial configurations is due to the fact that for these cases, the hydrodynamic interaction effects can be initially minimum (collinear configuration with a minimal point-to-point distance) and maximum (side-by-side configuration with a maximal point-to-point distance). Therefore, we consider two initial configurations: an identical pair of collinear, horizontally oriented fibers; and vertically oriented "side-by-side" fiber pairs. During sedimentation, the fibers deform and translate depending on gravitational forces, hydrodynamic interactions, elastic, and

27 January 2026 16:49:31

© Author(s) 2026

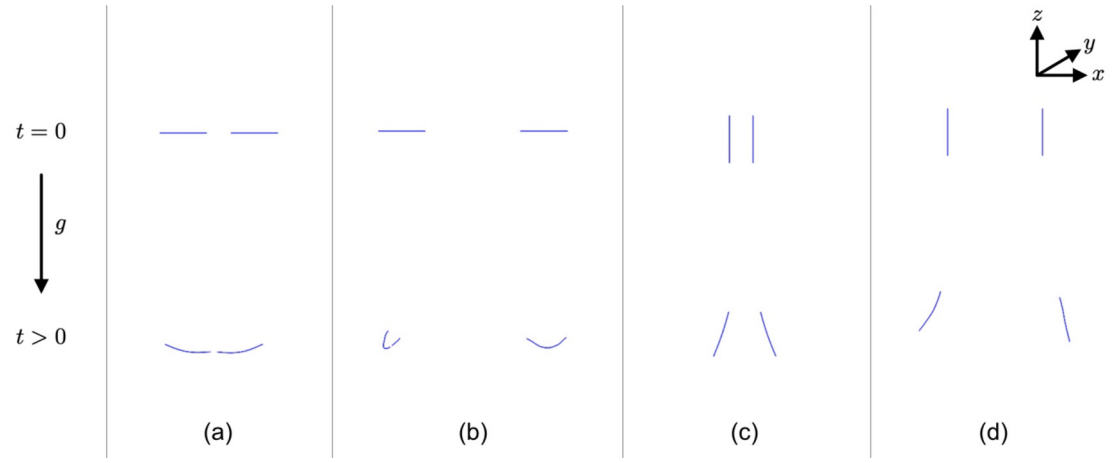

FIG. 3. Examples of fiber configurations at $t = 0$ (top) and at a later time (bottom) for each initial geometry, and for combinations of high and low gravitational Peclet number Pe_g, and small and large initial fiber separation. (a) Collinear initial geometry, small separation and high Pe_g. (b) Collinear geometry, large separation and low Pe_g. (c) Vertical configuration, small separation, and high Pe_g. (d) Vertical configuration, large separation, and low Pe_g.

Brownian forces. A triply periodic domain was used in which the ratio of domain length (L_d) to fiber length (l) was set to be 25. This is large enough to effectively eliminate the periodic artefacts.[26]

We first consider the overall behavior—thermally dominated vs hydrodynamic interaction-dominated—before quantifying the temporal dynamics. Validation of the numerical methodology is provided in Sec. A of the supplementary material.

A. Identification of sedimentation regime

Snapshots are given in Fig. 3 for both initial configurations, and for instances of high gravitational Peclet number Pe_g and initially nearby fibers, and conversely low Pe_g and large separation. These visually demonstrate the intuitive expectation that the former case will produce correlated motion dominated by hydrodynamic interactions, whereas the latter will instead generate uncorrelated motion dominated by thermal fluctuations.

The value of parameters considered in Fig. 3 can be found in Table I.

For each initial geometry, two scenarios were studied to help isolate the different physical mechanisms involved: (i) varying the initial fiber separation and Peclet number at fixed fiber stiffness; and (ii) varying the fiber stiffness and Peclet number at fixed initial fiber separation. We consider each in turn.

TABLE I. The physical parameters used in the simulations of case studies shown in Fig. 3.

Parameter	Value (a)	Value (b)	Value (c)	Value (d)
Pe_g	0.067 95	0.000 203 86	0.203 86	0.002 038 6
D^*	0.5	2.0	0.5	2.0
B^*	0.000 03	0.01	0.000 01	0.001
$\bar{t}$	10.0	18.3	6.0	9.1
ϵ		0.0046		
κ	3333.3	10	10 000	100

Since the fibers are subject to random thermal noise, 10 realizations were run for each set of case and the statistics reported as the average over this set of realizations. While this number is sufficiently large to determine the range of the differences between realizations, it does not give good statistics when these variations are large. However, we were not able to run larger numbers of realizations due to the computational expense of each simulation. As might be expected, the largest variations between realizations are found for vertical cases at low Peclet numbers and large separations where random fluctuations determine in which directions the fibers rotate.

1. Constant stiffness

In the first scenario, the bending stiffness was kept constant at $B^* = 100$, while the nondimensional initial inter-fiber separation (measured between their closest points) D^* was systematically varied from 0.2 to 2.0. The purpose of systematically changing the initial distance between fibers is to study both kinds of dilute and concentrated suspensions. The gravitational Peclet number Pe_g was varied from 2.02×10^{-5} to 6.74×10^{-2} for horizontal fibers and from 2.02×10^{-1} to 2.02×10^{-4} for vertical fibers. The aspect ratio was set to be 0.0046. The total simulation time $T_F^* = \frac{t}{\bar{t}}$ was set to 3000 to allow full capture of fiber dynamics. To give a more vivid picture of sedimentation process, we provide overlayed snapshots in real space in Fig. 4, which shows the evolution of fiber morphology during sedimentation, for fiber pairs starting from a collinear initial configuration in some sets of parameters.

Two metrics were employed to characterize the degree of correlated motion between the two fibers. Since the center of mass of an isolated non-Brownian fiber will fall vertically, motion in the x direction must result from either thermal fluctuations or hydrodynamic interactions. Correlations in the x-coordinates of the center of mass of each fiber were quantified by their normalized covariance ρ_{XX},

27 January 2026 16:49:31

© Author(s) 2026

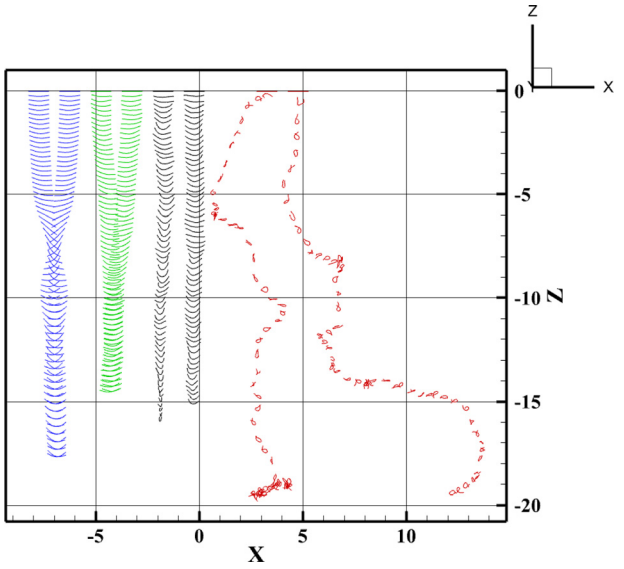

FIG. 4. Evolution of sedimentation of a fiber pair in the hydrodynamic interaction-dominated regime, starting from a collinear configuration, $B^* = 100$, $D^* = 0.5$ and various $Pe_g = 6.74 \times 10^{-2}$, 6.74×10^{-4}, 2.04×10^{-4}, 2.02×10^{-5} from left to right.

$$\rho_{XX} = \frac{cov(X_1, X_2)}{\sqrt{var(X_1)}\sqrt{var(X_2)}}, \tag{37}$$

where *cov* and *var* are, respectively, the covariance and variance of the x coordinates over the second half of total simulation time or until the fibers were observed to touch. In the case where fibers come into contact during sedimentation, we stopped the simulation at the time of contact and did not report results for later times. This choice is made purely to allow our discussion to focus on two physical mechanisms—thermal motion and hydrodynamic interactions—without introducing a third (excluded volume) that would complicate the interpretation of the results. Note that, at each time step, the *cov* and *var* are calculated over all 10 realizations and ρ_{XX} obtained from Eq. (37). Values of ρ_{XX} close to minus one correspond to trajectories, in which the fibers' horizontal translation was strongly anti-correlated during sedimentation, i.e., the hydrodynamic interactions dominated; conversely, values close to zero were interpreted as uncorrelated motion dominated by random thermal motion.

Mostly, it was found that the flexible fibers tend to converge toward horizontal and parallel orientation, as previously reported in Ref. 25. Figure 5 shows the variation of ρ_{XX} with Pe_g and D^* for both initial geometries. It is evident that for initially collinear fibers, hydrodynamic interactions dominate for high Pe_g and low D^*. This is reasonable, as it corresponds to cases where hydrodynamics interactions are expected to dominate over thermal fluctuations. However, for vertical fibers, there was no clear trend in this metric with large variations between neighboring points in parameter space. As mentioned above, this value has been calculated as an average over 10 realizations; however, inspection of individual simulations suggests that although there is some degree of correlation between the fibers, this is swamped by the variations between different realizations. While this could be addressed by running much larger ensembles to obtain better statistics, we instead considered a second statistical metric related to the orientation of fibers in the horizontal plane. More precisely, the end-to-end vectors of both fibers were projected into the horizontal x–y plane to give two-vectors $\boldsymbol{a}_1$ and $\boldsymbol{a}_2$, and the angular difference θ extracted as

$$\cos^2\theta = \frac{(\boldsymbol{a}_1 \cdot \boldsymbol{a}_2)^2}{|\boldsymbol{a}_1|^2 |\boldsymbol{a}_2|^2}. \tag{38}$$

Averaging over the same time window as before now shows a clear trend for vertical fibers as evident in Fig. 6. Fiber alignment $\theta \approx 0$ is again observed for high gravitational Peclet numbers, with this hydrodynamic interaction-dominated region becoming broader for smaller D^*, i.e., closer fibers. Conversely, the averaged $\cos^2\theta$ fluctuates around $\frac{1}{2}$, suggesting uncorrelated orientations, for low Peclet number and distant fibers, corresponding to thermally dominated motion as expected.

To illustrate further how the sedimentation behavior changes with the Peclet number at fixed fiber stiffness, Fig. 7 shows example trajectories for pairs of fibers at three different Peclet numbers. In the hydrodynamic interaction-dominated regime ($Pe_g = 2.04 \times 10^{-1}$), the

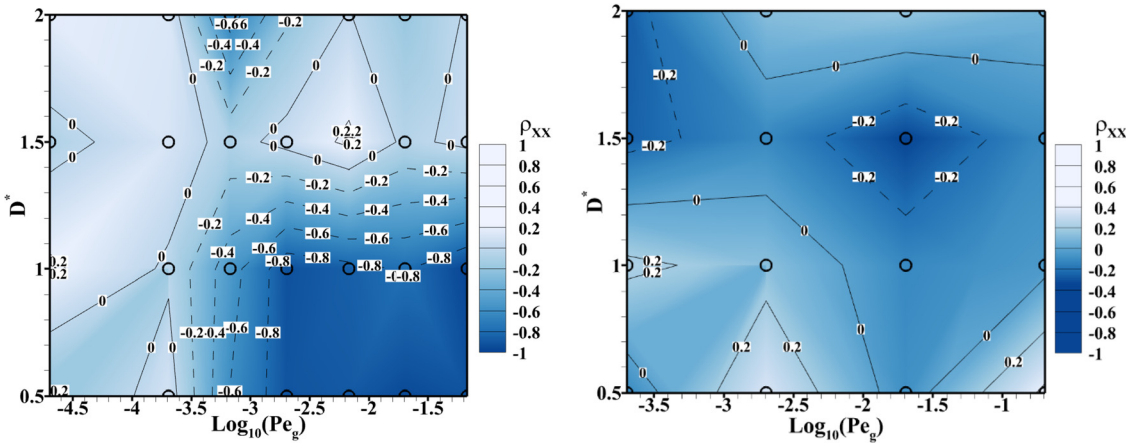

FIG. 5. The changes in ρ_{XX} due to variation in the gravitational Peclet number (Pe_g) and nondimensional initial distance (D^*) parameter, defined for a pair of initially collinear (left image) and side-by-side (right image) fibers.

27 January 2026 16:49:31

© Author(s) 2026

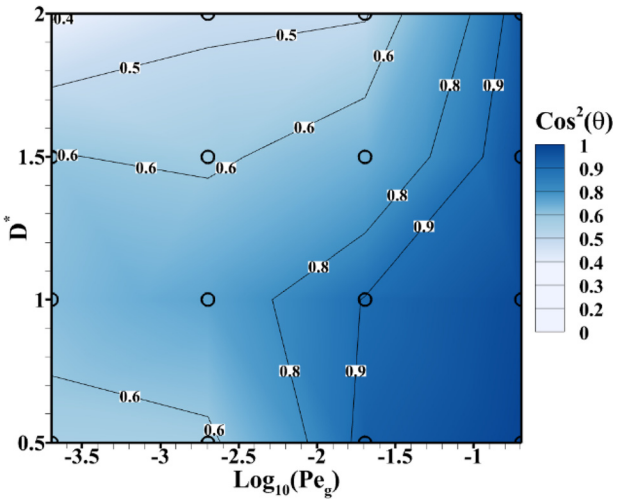

FIG. 6. Variation of the angular correlation metric $\cos^2\theta$ value for initially side-by-side vertical fibers.

fibers remain confined within the plane $y = 0$ and after the initial interaction move apart and fall in a slight U-shaped configuration, as in found for isolated fibers. At intermediate Peclet numbers, $Pe_g = 2.04 \times 10^{-3}$, thermal fluctuations affect the early part of the trajectory and can cause the fibers to rotate out the plane y = 0. In the case shown the pair become almost perpendicular when projected into the *xy* plane. At long times, they become separate and fall approximatively vertically in a U-shaped configuration. At even lower Peclet numbers, thermal fluctuations dominate over hydrodynamic interactions, and as a result, the fiber alignment is uncorrelated. Furthermore, the reduction in persistence length means that the fibers are more bent, which reduces the viscous drag and means that the fibers sediment faster than at larger Peclet numbers.

2. Controlled initial separation

For the second scenario, the initial distance between the fibers was fixed at an intermediate value $D^* = 1.0$ with the fiber stiffness (and hence persistence length) varied along with the Peclet number. More precisely, the fiber stiffness parameter κ was varied from 1 to 10^4, corresponding to the nondimensional parameter B^* varying from 1.0×10^{-1} to 1.0×10^{-5}, and Pe_g was varied from 2.02×10^{-4} to 2.02×10^{-1} for both geometries by varying the temperature. The chosen ranges of parameters were selected so that both regimes—hydrodynamic and thermal—were well covered for each study, which sometimes necessitated different values, especially for B^*. The aspect ratio (ϵ) was set at 0.0046, and the final simulation time was again $T_F^* = 3000$. The Reynolds number is around 0.1, based on the length of the fiber, which is small enough for the flow to be considered in the Stokes regime.

The orientation correlation metric $\cos^2\theta$ is presented in Fig. 8. For the collinear geometry, it can be seen that the hydrodynamic-dominated regime ($\cos^2\theta \approx 1$) corresponds to stiff fibers and low temperatures (higher Pe_g number), which is expected as stiff fibers do not readily contract and consequently the closest points between the pair are more likely to remain physically nearby, enhancing their hydrodynamic interaction. Hydrodynamic interactions are reduced for floppy fibers (low κ) as they retract their ends and hence increase their closest point of separation. Similar trends are observed for the vertical geometry, although the data are notably more noisy. It is also clear from the results shown in Fig. 8 that for the non-stiff fibers, the $\cos^2\theta$ value changes due to changes in the hydrodynamic interactions that can bring the fiber closer together or further apart, depending on the initial configuration of fibers.

B. Short time dynamics

As the dynamics of this system is quite complex, short and late time dynamics were considered separately, for each evaluating metrics

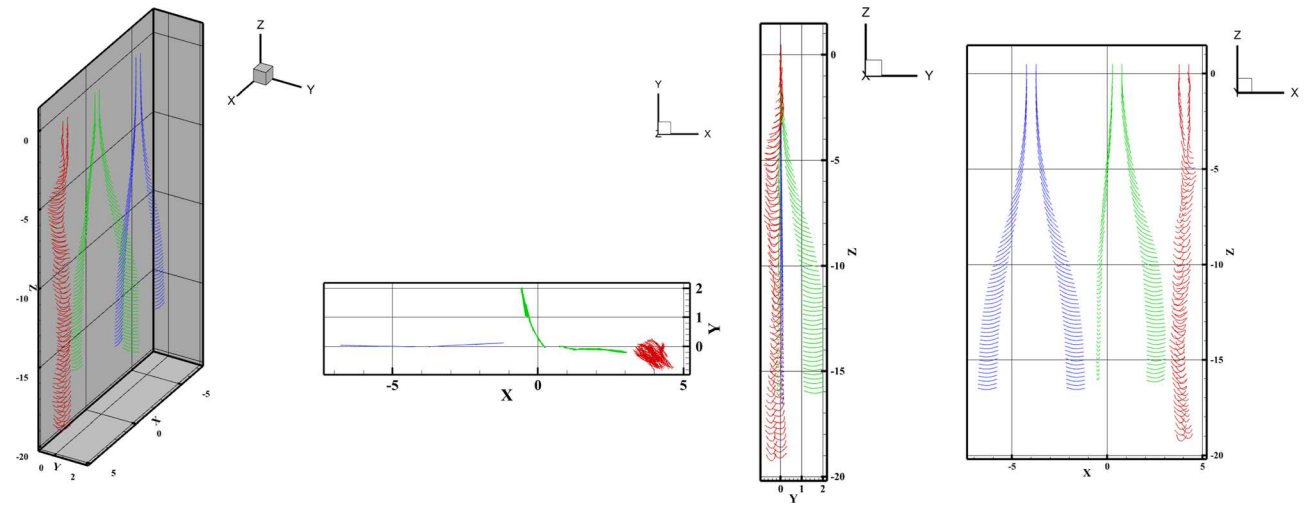

FIG. 7. Evolution of the configuration of a pair of sedimenting fibers started from a side-by-side configuration at $B^* = 100$, $D^* = 0.5$ for three different values of Pe_g : 2.04×10^{-1} (blue), 2.04×10^{-3} (green), and 2.04×10^{-4} (red). (Top left) the three-dimensional perspective, (top right) projection in the *xy* plane, (bottom left) projection in the *yz* plane, and (bottom right) projection in the *xz* plane.

27 January 2026 16:49:31

© Author(s) 2026

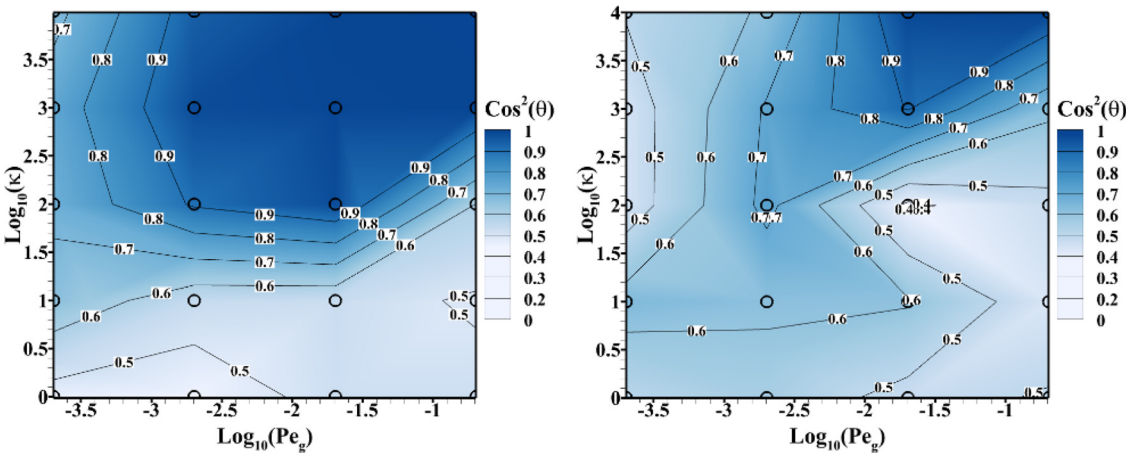

FIG. 8. Orientational correlations $\cos^2\theta$ varying the gravitational Peclet number Pe_g and the fiber stiffness κ, for a pair of initially horizontally collinear (left) and vertically side-by-side (right) fibers.

relevant to the observed qualitative behavior: rotation rate and net interaction velocity for the early dynamics, and sedimentation velocity and the gyration matric for late dynamics.

For short times, we can compare the rotation rate of the rods and the induced interaction velocity due to hydrodynamic interactions between the numerical results using the RPY approximation and the analytical calculations for continuum rods presented in Sec. III B. In the case of the simulations, both quantities were obtained by averaging the local values of rotation and velocity over the fiber lengths. Note that the interaction velocity was normalized with respect to the sedimentation velocity of a single horizontal fiber in the continuum model, and the rotation rate was normalized to the rotation rate of the smallest D^* considered for each configuration, also obtained from the continuum model. The simulations were performed at low temperature, $Pe_g = 202$, to better match the assumptions of the continuum model, and for the same reason, the bending stiffness was chosen to approximate rigid fibers ($B^* = 0.1$ in our units).

The initial velocities and rotation rates as a function of the normalized separation D^* are presented in Figs. 9 and 10, for collinear and vertical fibers, respectively. There is a good agreement between the continuum prediction and numerical results. However, in Fig. 10, there is a discrepancy at small D^*. This is due to the difference in the mobility kernels employed, i.e., RPY vs Oseen, especially for the vertical fibers for which the hydrodynamic interaction effects can be initially maximum (side-by-side configuration with a maximal point-to-point distance). The discrepancies found at large D^* for both Figs. 9 and 10 arise from the effects of periodic boundary conditions that are present in the RPY simulations but not in the analytical calculations. At large separations, the fibers become closer to the periodic images of each other, which results in an increased interaction not found in the analytical calculations.

There is also a consistent difference between the data for the interaction velocity for this geometry. We attribute these deviations to the difference in the mobility kernels employed, i.e., RPY vs Oseen, which become more pronounced in this vertical configuration as in this case the entire all lengths of both fibers (as opposed to just one end of each) are in close proximity to each other.

C. Long time dynamics

In all cases, at long times, the sedimentation velocity eventually reached a steady state in which the gravitational force is balanced by

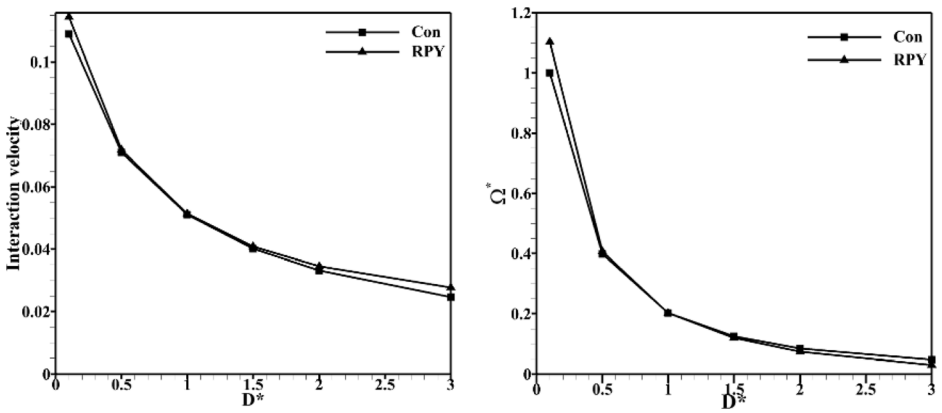

FIG. 9. Comparison of the predictions of the numerical RPY model (delta) and the analytical continuum model (square) for the nondimensional interaction velocity values (left) and nondimensional rate of rotation (right), against the nondimensional distance paramter (D^*), for a pair of initially horizontal and colinear fibres.

27 January 2026 16:49:31

© Author(s) 2026

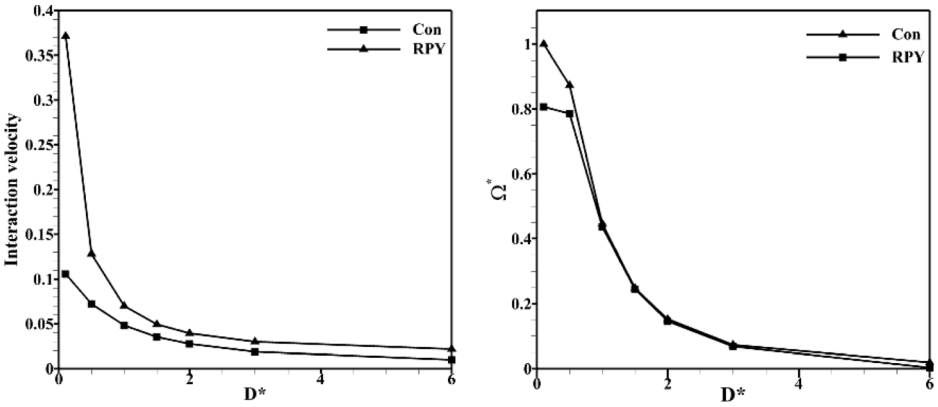

FIG. 10. Comparison of the predictions of the numerical RPY model (delta) and the analytical continuum model (square) for the nondimensional interaction velocity values (left) and nondimensional rate of rotation (right), against the nondimensional distance parameter (D^*), for a pair of initially vertical fibers.

the hydrodynamic force averaged over the fiber configuration, with the time to reach the statistical steady state depending on system parameters. In this section, the sedimentation velocity and the fiber configuration represented by the gyration tensor I are reported. In Stokes flow, the hydrodynamic resistance scales with the largest linear dimension of the body, which can be estimated from the largest eigenvalue of the gyration tensor defined as[13]

$$I = 1/l \int_0^l \left(\mathbb{X}(s) - \bar{\mathbb{X}}\right)^2 ds, \tag{39}$$

where $\bar{\mathbb{X}}$ is the position of the center of mass of the fiber defined as

$$\bar{\mathbb{X}} = 1 \Big/ l \int_0^l \mathbb{X}(s) ds. \tag{40}$$

The sedimentation velocity and eigenvalues of the gyration matrix for the collinear horizontal configuration, for both constant stiffness and controlled initial distances, are given in Fig. 11. These values are recorded either at the end of simulation time, or when the fibers touch each other. The error bars indicate the range of variation of sedimentation velocity amongst the 10 different realizations.

For fibers that are sufficiently stiff to remain approximately straight, the sedimentation velocity depends upon orientation of the fiber with respect to gravity between the extremes of vertical and horizontal orientations. The velocities corresponding to these two cases are shown as horizontal lines in Figs. 10(a) and 10(b). Figure 11(a) shows how the sedimentation velocity varies with Pe_g for a constant fiber stiffness, $B^* = 100$. The sedimentation velocity is higher and noisier (larger error bars) at small Peclet number and for large separations decreases in value (and becomes less noisy) as Pe_g increases and sediment at a speed close to that of isolated horizontal fibers. However, for smaller separations, this initial decrease is followed by an increase in sedimentation velocity with Pe_g as the system crosses-over into the hydrodynamic interaction-dominated regime. Although there is some decrease in the drag on a pair of fibers compared to that on two isolated fibers, this increase is mainly due to the rotation of the fibers. In all cases, the sedimentation velocity remains approximately within the bounds corresponding to a single vertical (low drag) and horizontal (high drag) fiber.

Figure 11(b) shows the effect of varying fiber stiffness for a fixed initial distance ($D^* = 1.0$). The sedimentation velocity is higher for softer fibers ($L_p = 1.0$), as their flexibility allows them to bend into shapes with lower drag.

Turning to the gyration tensor, the three eigenvalues are presented in Fig. 11(c) for the cases of varying Pe_g at a fixed fiber stiffness. The eigenvector corresponding to the largest eigenvalue is approximately aligned with the z axis, suggesting fibers sediment in approximately vertical configurations at late times. The error bars indicate the range of variation of eigenvalues between different realizations. In addition, at small Pe_g, the largest eigenvalue is smaller than at large Pe_g, especially at smaller initial separations, consistent with Brownian forces acting to reduce the fiber end-to-end length as the persistence length decreases. Note that at constant B^* decreasing the Peclet number reduces the persistence length. Figure 11(d) appears to show the opposite trend, with the largest eigenvalue decreasing with the Peclet number for fibers with a persistence length $l_p = 10^4$. However, for a fixed value of l_p, the value of B^* decreases as the Peclet number increases, so these fibers bend due to hydrodynamic forces.

The corresponding data for the initially vertical side-by-side geometry is presented in Fig. 12. Similar to the collinear configuration, the sedimentation velocity for the fiber pair remains between those of a single horizontal and vertical rigid fiber. However, unlike the collinear case, initially close fibers do not fall faster than those with a larger initial separation, nor does the initial separation appear to affect the form of the gyration tensor. This is because of the fact that there is a competition between hydrodynamic interaction and Brownian motion depending on both the Pe_g and D^*. Comparing Figs. 11(a) and 11(c) with Figs. 12(a) and 12(c), we observe that all the initially vertical cases resemble the cases of the well-separated horizontal fibers. In all these cases, the fibers eventually fall as individual fibers, whereas closely separated collinear fibers fall as pairs as can be seen in Fig. 3(a). The results of varying fiber stiffness shown in Figs. 12(b) and 12(d) are qualitatively similar to those found for the initially collinear fibers. Brownian motion again enhances sedimentation by contracting the fiber and reducing the overall drag.

V. CONCLUSION

The sedimentation of fibers is a central process in the synthesis of a range of important materials, but the complexity of the problem means that it is often challenging to predict in advance the geometry and conformation of the fibers once they are deposited onto a substrate. This lack of accurate predictive capability means that optimal

27 January 2026 16:49:31

© Author(s) 2026

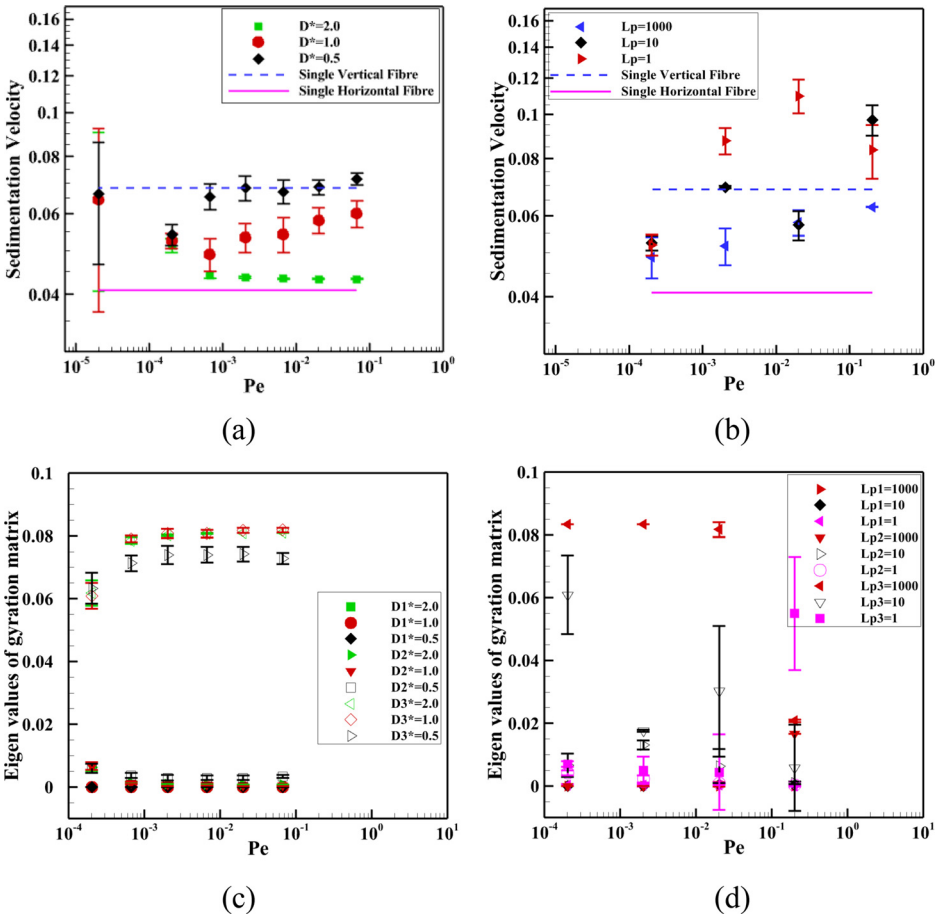

FIG. 11. The sedimentation velocity [top row, (a) and (b)] and the three eigenvalues of the gyration matrix labeled 1, 2, and 3 in the legend [bottom row, (c) and (d)] for both controlled initial distance [left column (a) and (c)] and constant stiffness [right column, (b) and (d)] scenarios for initially horizontal collinear fibers.

formulations for any target application must be found empirically, requiring lengthy experimental assays, and running the risk of missing optimal parameter combinations due to the limited understanding of the underlying physical mechanisms. Mathematical modeling can provide this predictive power, but suitably accurate models are not trivial to develop when all three of fiber elasticity, thermal fluctuations, and hydrodynamic interactions, need to be included. Here, we have adopted a recent numerical implementation of Rotne–Prager–Yamakawa (RPY) kernels to systematically vary the relative strengths of all three of these mechanisms for the simplest situation when hydrodynamic interactions are relevant, that is, pairs of fibers. We have identified when hydrodynamic interactions dominate over thermal fluctuations and vice versa, and characterized the temporal dynamics at both short and long times, starting from two classes of initial geometry. In all cases, our findings have been intuitively justified based on the relative influence of the physical processes involved. It was found that, for collinear configuration, the sedimenting fibers move toward each other within the sedimentation plane (xz plane) at high Pe number and when the fibers are close enough to each other (due to dominance of hydrodynamic interaction), while at low Pe number, the fibers move randomly in different directions (out-of-plane translation) as they sediment (due to the dominance of thermal fluctuations). For side-by-side configuration, the fibers rotate in the sedimentation plane (xz plane) at high Pe number and when the fibers are close enough to each other as they sediment (again due to the dominance of hydrodynamic interaction), whereas at low Pe number and when the fibers are far from each other, they randomly rotate in different directions (out of plane rotation) (again due to the dominance of thermal fluctuations).

Bead modeling and related schemes provide a smaller obstacle to developing numerical models than RPY, but come with a limitation on the aspect ratio of the fibers that can be represented. In bead models, extreme aspect ratios (i.e., long thin fibers) necessitate many beads per fiber, which becomes numerically expensive to simulate as the number of fibers increases: Real fibers are often hundreds of times longer than their radius, requiring hundreds of beads to represent a single fiber, so many-fiber systems could easily require 10^4 or more beads to be integrated in time. Compared to full slender body theory with ill-posedness problem and bead model with hundreds of beads, the non-singular RPY can achieve similar aspect ratios with much fewer discrete points as in Fig. 2 (our results correspond to $\epsilon = 0.0046$, i.e., fibers about 217 times longer than their radius) plus the integration techniques (the quadrature), resulting in lower efficient computational demands to accurately predict fiber dynamics. The trade-off is the

27 January 2026 16:49:31

© Author(s) 2026

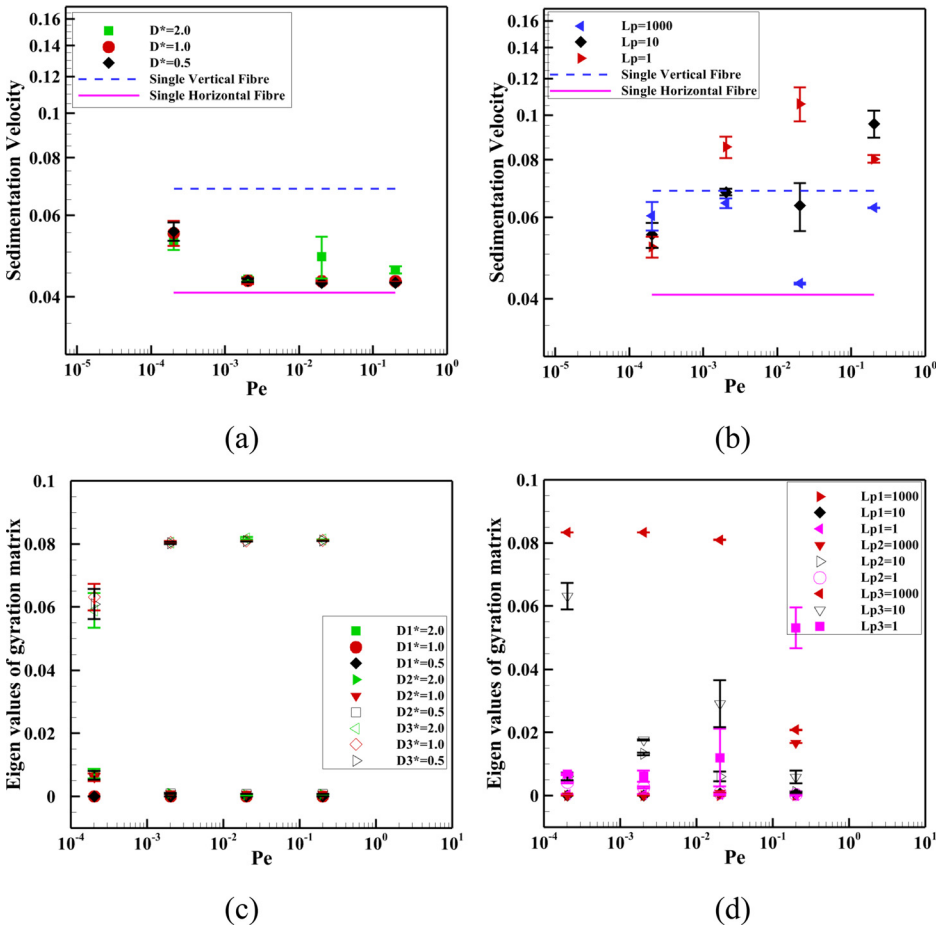

FIG. 12. The sedimentation velocity [top row (a) and (b)] and the eigenvalues of gyration matrix labeled 1, 2, and 3 in the legend [bottom row (c) and (d)] for both controlled initial distance [left column (a) and (c)] and constant stiffness [right column (b) and (d)] scenarios for the vertical side-by-side fiber configuration.

higher development time required, but this is overcome by the use of open-source software that has already overcome these challenges, which is the approach we have adopted here.

In this work, fiber pairs were chosen as the minimum number of fibers for which hydrodynamic interactions are relevant, but it is straightforward to extend our approach to any number of fibers. This would require consideration of suitable initial geometries, such as some form of randomly defined orientations and positions, or an ordered geometry, as befits the application. Suitable metrics would also need to be selected that are relevant to many-fiber systems, although we suggest those employed here, that quantify the degree of correlation and fiber conformation, make suitable starting points for more general quantities that still have the potential to generate significant insight into the problem. For example, it is not clear how the hydrodynamic interaction (velocity fluctuations) affects the Brownian motion as time passes and needs to be further addressed by the use of some other metrics such as auto-correlations functions in the future.[35]

SUPPLEMENTARY MATERIAL

See the supplementary material for details. The accuracy of the numerical framework has been verified against established benchmarks. In particular, the results were validated for Jeffery orbits of a single fiber in shear flow and for the sedimentation dynamics of an isolated fiber. These validation tests, together with detailed comparisons, are provided in the supplementary material.

ACKNOWLEDGMENTS

This work was funded by an EPSRC UK DTP Scholarship Award.

AUTHOR DECLARATIONS

Conflict of Interest

The authors have no conflicts to disclose.

Author Contributions

Nasrollah Hajaliakbari: Methodology (equal); Validation (equal); Writing – original draft (equal); Writing – review & editing (equal). **David Head:** Supervision (equal); Writing – review & editing (equal). **Oliver Harlen:** Supervision (equal); Writing – review & editing (equal).

DATA AVAILABILITY

The data that support the findings of this study are available within the article and its supplementary material.

27 January 2026 16:49:31

© Author(s) 2026

REFERENCES

[1]E. Young, D. Martinez, J. Olson, K. Buckley, S. Jivan, T. Ruth, and V. Sossi, "The sedimentation of papermaking fibers," AlChE. J. **52**, 2697 (2006).
[2]O. J. Rojas and M. A. Hubbe, "The dispersion science of papermaking," J. Dispersion Sci. Technol. **25**, 713 (2005).
[3]X. Xu and A. Nadim, "Deformation and orientation of an elastic slender body sedimenting in a viscous liquid," Phys. Fluids **6**, 2889 (1994).
[4]B. Marchetti, V. Raspa, A. Lindner, O. Du Roure, L. Bergougnoux, É. Guazzelli, and C. Duprat, "Deformation of a flexible fiber settling in a quiescent viscous fluid," Phys. Rev. Fluids **3**, 104102 (2018).
[5]D. R. Hewitt, D. T. Paterson, N. J. Balmforth, and D. M. Martinez, "Dewatering of fibre suspensions by pressure filtration," Phys. Fluids **28**, 063304 (2016).
[6]B. Herzhaft, É. Guazzelli, M. B. Mackaplow, and E. S. Shaqfeh, "Experimental investigation of the sedimentation of a dilute fiber suspension," Phys. Rev. Lett. **77**, 290 (1996).
[7]B. Herzhaft and É. Guazzelli, "Experimental study of the sedimentation of dilute and semi-dilute suspensions of fibres," J. Fluid Mech. **384**, 133 (1999).
[8]S. F. Schoeller, A. K. Townsend, T. A. Westwood, and E. E. Keaveny, "Methods for suspensions of passive and active filaments," J. Comput. Phys. **424**, 109846 (2021).
[9]B. Marchetti, "Sédimentation de particules: Effets collectifs et filaments déformables," Ph.D. thesis (ILO, 2018).
[10]L. Li, H. Manikantan, D. Saintillan, and S. E. Spagnolie, "The sedimentation of flexible filaments," J. Fluid Mech. **735**, 705 (2013).
[11]E. Tozzi, C. Scott, D. Vahey, and D. Klingenberg, "Settling dynamics of asymmetric rigid fibers," Phys. Fluids **23**, 033301 (2011).
[12]O. Maxian and A. Donev, "A simulation platform for slender, semiflexible, and inextensible fibers with Brownian hydrodynamics and steric repulsion," Phys. Fluids **36**, 123320 (2024).
[13]L. H. Cunha, J. Zhao, F. C. MacKintosh, and S. L. Biswal, "Settling dynamics of Brownian chains in viscous fluids," Phys. Rev. Fluids **7**, 034303 (2022).
[14]M. Cosentino Lagomarsino, I. Pagonabarraga, and C. Lowe, "Hydrodynamic induced deformation and orientation of a microscopic elastic filament," Phys. Rev. Lett. **94**, 148104 (2005).
[15]B. Delmotte, E. Climent, and F. Plouraboué, "A general formulation of Bead Models applied to flexible fibers and active filaments at low Reynolds number," J. Comput. Phys. **286**, 14 (2015).
[16]G. Batchelor, "Slender-body theory for particles of arbitrary cross-section in Stokes flow," J. Fluid Mech. **44**, 419 (1970).
[17]B. Altunkeyik, A. Rahmat, and T. Montenegro-Johnson, "Dynamics of active poroelastic filaments in Stokes flow," Phys. Rev. E **111**, 025421 (2025).
[18]I. Llopis, I. Pagonabarraga, M. Cosentino Lagomarsino, and C. P. Lowe, "Sedimentation of pairs of hydrodynamically interacting semiflexible filaments," Phys. Rev. E **76**, 061901 (2007).
[19]G. Saggiorato, J. Elgeti, R. G. Winkler, and G. Gompper, "Conformations, hydrodynamic interactions, and instabilities of sedimenting semiflexible filaments," Soft Matter **11**, 7337 (2015).
[20]K. Gustavsson and A.-K. Tornberg, "Gravity induced sedimentation of slender fibers," Phys. Fluids **21**, 123301 (2009).
[21]E. Nazockdast, A. Rahimian, D. Zorin, and M. Shelley, "A fast platform for simulating semi-flexible fiber suspensions applied to cell mechanics," J. Comput. Phys. **329**, 173 (2017).
[22]J. Park, B. Metzger, E. Guazzelli, and J. E. Butler, "A cloud of rigid fibres sedimenting in a viscous fluid," J. Fluid Mech. **648**, 351 (2010).
[23]M. Gruziel-Słomka, P. Kondratiuk, P. Szymczak, and M. L. Ekiel-Jeżewska, "Stokesian dynamics of sedimenting elastic rings," Soft Matter **15**, 7262 (2019).
[24]M. Gruziel, K. Thyagarajan, G. Dietler, A. Stasiak, M. L. Ekiel-Jeżewska, and P. Szymczak, "Periodic motion of sedimenting flexible knots," Phys. Rev. Lett. **121**, 127801 (2018).
[25]M. Bukowicki and M. L. Ekiel-Jeżewska, "Sedimenting pairs of elastic microfilaments," Soft Matter **15**, 9405 (2019).
[26]O. Maxian and A. Donev, "A simulation platform for slender, semiflexible, and inextensible fibers with Brownian hydrodynamics and steric repulsion," arXiv:2408.15913 (2024).
[27]O. Maxian, A. Donev, and A. Mogilner, "Interplay between Brownian motion and cross-linking controls bundling dynamics in actin networks," Biophys. J. **121**, 1230 (2022).
[28]O. Maxian, *Hydrodynamics of Transiently Cross-Linked Actin Networks: Theory, Numerics, and Emergent Behaviors* (New York University, 2023).
[29]O. Maxian, R. P. Peláez, A. Mogilner, and A. Donev, "Simulations of dynamically cross-linked actin networks: Morphology, rheology, and hydrodynamic interactions," PLoS Comput. Biol. **17**, e1009240 (2021).
[30]S. Delong, B. E. Griffith, E. Vanden-Eijnden, and A. Donev, "Temporal integrators for fluctuating hydrodynamics," Phys. Rev. E **87**, 033302 (2013).
[31]R. P. Peláez, *Complex Fluids in the GPU Era: Algorithms and Simulations* (Universidad Autónoma de Madrid, 2022).
[32]O. Maxian, A. Mogilner, and A. Donev, "Integral-based spectral method for inextensible slender fibers in Stokes flow," Phys. Rev. Fluids **6**, 014102 (2021).
[33]W. Chester, "On Oseen's approximation," J. Fluid Mech. **13**, 557 (1962).
[34]M. Doi, S. F. Edwards, and S. F. Edwards, *The Theory of Polymer Dynamics* (oxford university Press, 1988).
[35]F. R. Cunha and E. J. Hinch, "Shear-induced dispersion in a dilute suspension of rough spheres," J. Fluid Mech. **309**, 211 (1996).

27 January 2026 16:49:31

© Author(s) 2026